RSC Advances

PAPER

View Article Online
View Journal | View Issue

Cite this: *RSC Adv.*, 2019, **9**, 38597

Effect of extremely high CO_2 pressure on the formation of the corrosion film on 13Cr stainless steel

Jinyang Zhu,[a] Dapeng Li,*[b] Yunan Zhang[a] and Lei Zhang *[c]

Received 14th October 2019
Accepted 8th November 2019

DOI: 10.1039/c9ra08373a

rsc.li/rsc-advances

The corrosion behaviors of 13Cr martensitic steel under different CO_2 partial pressures (4–28 MPa) were investigated by weight loss tests and surface characterizations. The results show that the corrosion rate of 13Cr steel shows a sharp increase under higher CO_2 pressure (28 MPa), which reached approximately 20–180 times as large as those under lower CO_2 pressures (4–12 MPa). Under the lower CO_2 pressures, a single-layered $Cr(OH)_3$ passive film forms and completely covers the steel surface. However, when the CO_2 pressure reaches 28 MPa, a very different corrosion film which contains an inner $Cr(OH)_3$ passive layer and an outer $FeCO_3$ layer forms, and the inner passive layer shows local damage. This phenomenon can be explained by the lower pH (~2.75) and the higher H_2CO_3 concentration in the solution under the higher CO_2 pressure.

Introduction

CO_2 corrosion is becoming a more and more severe concern in the oil and gas industry as a result of the increasing CO_2 concentration with numerous oil and gas fields entering the later development period, as well as the wide use of the CO_2 enhanced oil recovery (EOR) technique.[1–3] Carbon steels (CS) or low alloy steels (LAS), such as J55, N80, P110, 1Cr, 3Cr, and 5Cr, have been widely used for downhole tubing due to their low cost. However, their poor CO_2 corrosion resistance has caused a lot of failures and brought huge economic losses. Furthermore, the leakage of oil and gas can also cause great environmental pollution. Corrosion resistant alloys (CRA) including martensitic, ferritic, austenitic and duplex stainless steels, as well as nickel and cobalt alloys and other alloys, will be used in the upstream oil and gas environment when the use of carbon or low alloy steels is not economical due to the presence of either CO_2 or H_2S.[4]

Among these CRAs, 13Cr martensitic stainless steel is the most widely used to increase the service life of tubing.[5–9] The tubing which serves in a high salinity solution with high-temperatures and high-pressures can undergo severe general corrosion or localized/pitting corrosion.[10–15] 13Cr stainless steel has been proved to have the good corrosion resistance in CO_2 environments as long as the temperature is lower than 150 °C,[16] and also a higher strength and a lower cost than the other CRAs such as duplex stainless steels.[10,17,18] A lot of researches have studied the corrosion resistance of 13Cr stainless steel and the effect of temperature, chloride ion, and sulphide ion on the passive film stability of 13Cr steel in CO_2 environments.[11,19–25] However, it is unclear how the presence of CO_2 affects the corrosion behaviours of 13Cr stainless steel, particularly the stability of passive films under ultra-high CO_2 partial pressures. Do the CO_2 act as an inhibitor for the corrosion of 13Cr steel? Or do the extreme high CO_2 partial pressures increase the susceptibility of 13Cr steel to localized/pitting corrosion? Several studies have investigated the localized/pitting corrosion mechanism of stainless steel in CO_2 environments under the CO_2 partial pressures that are not higher than 10 MPa.[13,26–30] However, limited studies have reported the relationship between the extremely high partial pressure of CO_2 (above 20 MPa), stability of passive film, and pitting corrosion of 13Cr stainless steel.

The objective of this work is to explore the effect of partial pressures of CO_2 (up to 28 MPa) on the corrosion of 13Cr stainless steel and clarify how the presence of CO_2 affect the stability of passive film under different CO_2 partial pressures against pitting corrosion. Scanning electron microscopy (SEM), X-ray diffraction (XRD), quadrant back scattering detector (QBSD), energy dispersive X-ray spectroscopy (EDS), and X-ray photoelectron spectroscopy (XPS) were conducted to investigate the surface and cross-sectional morphology and composition of the corrosion film that forms on the steel surface. A detailed calculation on the pH values and phase concentrations of the test solutions was carried out to investigate the influence of CO_2 partial pressures on the stability of passive film and the formation of the corrosion film on 13Cr stainless steel surface in CO_2 environments.

[a]*National Center for Materials Service Safety, University of Science and Technology Beijing, Beijing 100083, PR China*

[b]*CNOOC Research Institute, Beijing 100028, PR China*

[c]*Corrosion and Protection Center, University of Science and Technology Beijing, Beijing 100083, PR China. E-mail: Zhanglei@ustb.edu.cn*

Experimental

Weight loss tests

The immersion tests of 13Cr martensitic steel under different CO_2 partial pressures were carried out in a 5 L autoclave. The composition of the test solution is listed as follows (mg L^{-1}): 36.3 Ca^{2+}, 10.2 Mg^{2+}, 3838 $K^+ + Na^+$, 9008 Cl^-, 181.5 SO_4^{2-}, and 3207 HCO_3^-. Prior to each test, the specimen was weighed using an analytical balance to get the original weight. After the immersion of 480 h, the corroded specimens extracted from the autoclave were immediately rinsed with absolute ethyl alcohol. The corrosion products were removed according to ASTM G1-03 standard,[31] then rinsed, dried, and reweighed to determine the final weight of the specimen. The average corrosion rate was calculated using the following equation.

$$C_i = \frac{87600(W_{0i} - W_{1i})}{t\rho S}; \quad (i = 1, 2\ldots) \tag{1}$$

where C_i is the average corrosion rate, mm per year; W_{0i} and W_{1i} are the original and final weight of specimen, g, respectively; t is immersion time, h; ρ is the density of steel, g cm^{-3}; and S is the exposed surface area in cm^2.

Prior to each test, the solution was deaerated and carbonated by bubbling ultrapure CO_2 (99.999%) with a flow rate of 100 mL (L^{-1} min^{-1}) for at least 12 h. Six parallel samples hanged by a glass holder were immersed into the solution as soon as the solution was put into the autoclave. Two more hours of CO_2 pure was carried out to remove the oxygen mixed in the process of solution transfer after the autoclave was closed. The immersion tests were performed under 140 °C and different CO_2 partial pressures (4 MPa, 8 MPa, 12 MPa, and 28 MPa). The pressure was raised by using a booster pump. The temperature and the pressure simulated the production condition of an oil field in the East China Sea.

Morphology observation and composition analysis

The surface morphology and composition of the corrosion film were investigated by using SEM coupled with EDS, XRD, and XPS using an Al Kα (ht = 1486.6 eV) X-ray source. The cross-sectional morphology was observed by using the QBSD technique.

Electrochemical measurements

The electrochemical characterization was carried out in a homemade 5 L autoclave with the conventional three-electrode system at 140 °C. The 13Cr specimen was used as a working electrode (WE), a platinum sheet was used as a counter electrode (CE), and a high-temperature and high-pressure Ag/AgCl probe was used as a reference electrode (RE). The cyclic potentiodynamic polarization measurements were carried out to investigate the pitting corrosion and passivation behavior at different CO_2 pressures. Prior to the cyclic potentiodynamic polarization measurements, the open circuit potential (OCP) was stabilized for at least 1 h. The polarization curves were recorded from −100 mV (*vs.* OCP) to +1500 mV in the positive direction at a scan rate of 0.5 mV s^{-1}.

Results

Corrosion rates obtained by weight loss tests

The conclusions section should come in this section at the end of the article. Fig. 1 illustrates that the average corrosion rate is positively correlated to CO_2 partial pressure. The corrosion rate is very low (<0.0005 mm per year) and almost no corrosion occurs on 13Cr steel when the CO_2 partial pressure is below 12 MPa. When the pressure reaches 28 MPa, the corrosion rate shows a sharp increase and reaches about 0.01 mm a^{-1}, which is approximately 20–180 times as large as those under the lower CO_2 partial pressures.

Morphologies and composition of the corrosion film

As shown in Fig. 2a, there is no obvious corrosion product on the surface of 13Cr steel after immersion for 480 h under the CO_2 pressure of 4 MPa. Even the scratches caused by polish of samples before immersion tests are clearly visible. The corrosion morphology of 13Cr steel under the CO_2 pressure of 8 MPa (Fig. 2b) is similar with that under 4 MPa. When the pressure reaches 12 MPa, a few scattered particles start to form on the steel surface as shown in Fig. 2c. If the pressure continues to increase, a large amount of corrosion products which are stacked in grain shape form on the steel surface (Fig. 2d). In the enlarged photograph, these corrosion product particles have a typical crystal characteristic. This type of corrosion film allows corrosive ions pass through, and thus it is less protective than the dense amorphous film.[32,33]

A thin passive film probably forms on the substrate surface. Fig. 3 gives the XPS spectra of Cr 2p signals recorded for the corrosion film that forms on 13Cr steel surface under the lower CO_2 partial pressures of below 12 MPa. As shown in Fig. 3a, the Cr 2p spectrum of the corrosion film under 4 MPa is composed of two sets of peaks corresponding to $2p_{1/2}$ (586.8 eV) and $2p_{3/2}$ (577.0 eV), representing $Cr(OH)_3$.[34,35] The Cr 2p spectra of the corrosion film under 8 MPa (Fig. 3b) and 12 MPa (Fig. 3c) are similar with that under 4 MPa, both corresponding to $Cr(OH)_3$. To confirm the state of this $Cr(OH)_3$ film, an XRD investigation was conducted in this section. Fig. 3d shows the XRD spectra of

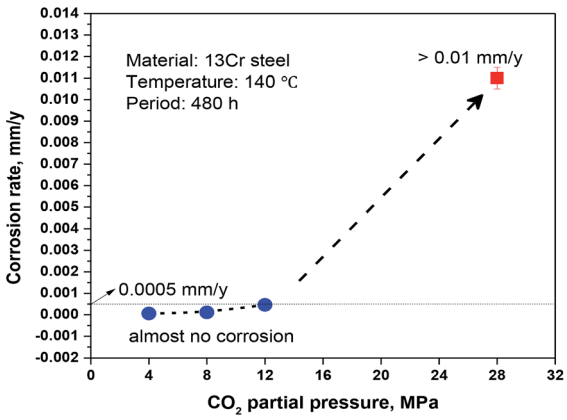

Fig. 1 Average corrosion rates of 13Cr stainless steel under different CO_2 partial pressures.

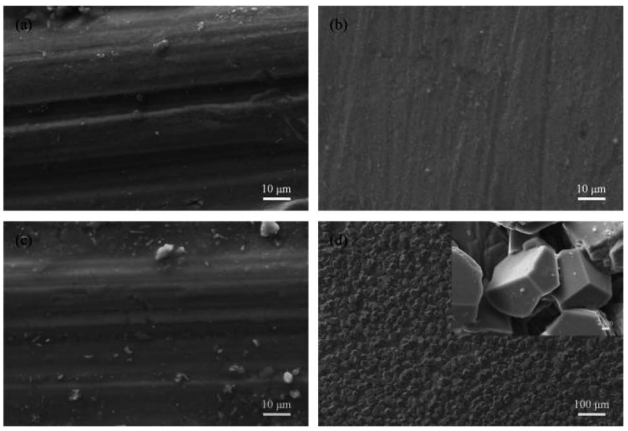

Fig. 2 Surface morphologies of 13Cr stainless steel after an immersion for 480 h in oilfield formation waters under 140 °C and different CO_2 partial pressures: (a) 4 MPa; (b) 8 MPa; (c) 12 MPa; (d) 28 MPa.

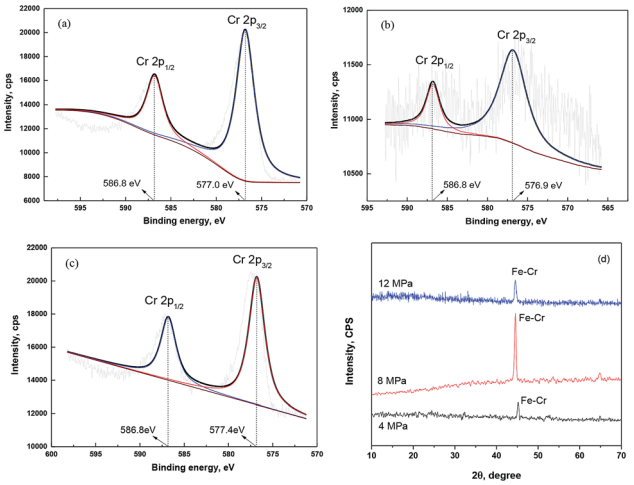

Fig. 3 XPS (a–c) and XRD (d) spectra of Cr 2p signals recorded for the corrosion film that forms on 13Cr steel surface under different CO_2 partial pressures: (a) 4 MPa; (b) 8 MPa; (c) 12 MPa.

the corrosion film that forms on 13Cr steel surface under the lower CO_2 partial pressures of below 12 MPa. As shown in Fig. 3d, only one peak located at 45° is observed in the spectra. This peak is the characteristic spectral lines for Fe–Cr. Moreover, some bulges are found on the spectra, which represent the amorphous state of the corrosion film. In summary, it can be suggested that a thin amorphous $Cr(OH)_3$ passive film forms on the 13Cr steel surface when the CO_2 partial pressure is not higher than 12 MPa. Therefore, it shows a very low corrosion rate under the lower CO_2 pressures in Fig. 1 as a result of the good protection from the dense amorphous passive film.

Fig. 4 gives the cross-section morphologies and EDS line scanning analysis of the corrosion film on 13Cr steel surface after an immersion for 480 h in an oilfield formation water under 140 °C and 28 MPa. As shown in Fig. 4a, the corrosion film on substrate surface shows two different regions; region A and region B. In region B (as shown in Fig. 4b), the corrosion

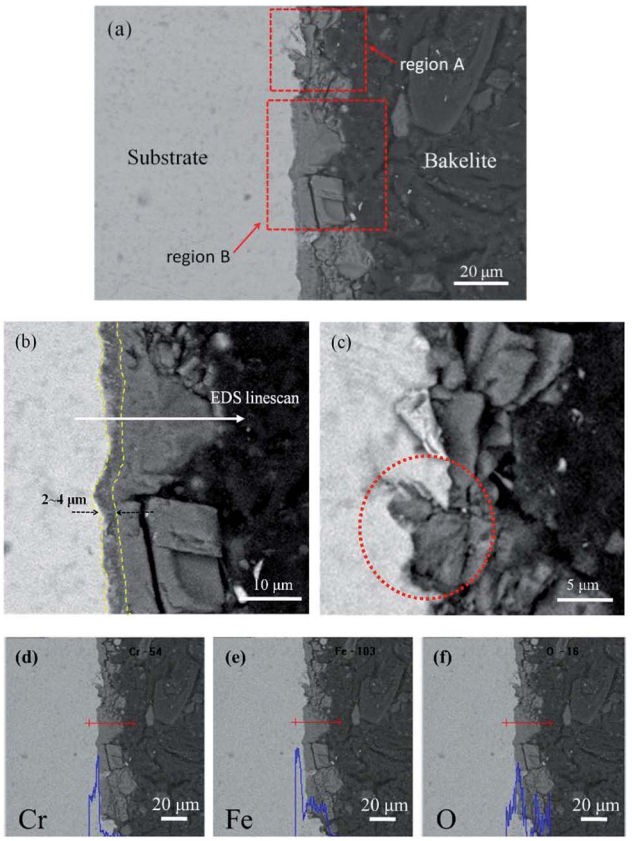

Fig. 4 Cross-section morphologies (a–c) and EDS line scanning analysis of Cr (d), Fe (e) and O (f) for corrosion film under 28 MPa.

film can be divided into two layers; an inner dense layer of about 2–4 μm and an outer porous layer of about 15–20 μm. The EDS line scanning analysis (Fig. 4d) shows that Cr is much enriched in the inner layer. The inner layer mainly consists of Cr and O. The O/Cr atomic ratio is about 2.8, which is nearly 3, indicating that the inner layer is probably $Cr(OH)_3$. In the outer layer, no Cr is found. The O/Fe atomic ratio is about 3, most likely indicating the presence of $FeCO_3$. The XRD result (Fig. 5) on the surface of corrosion film further proves the presence of $FeCO_3$ in the outer

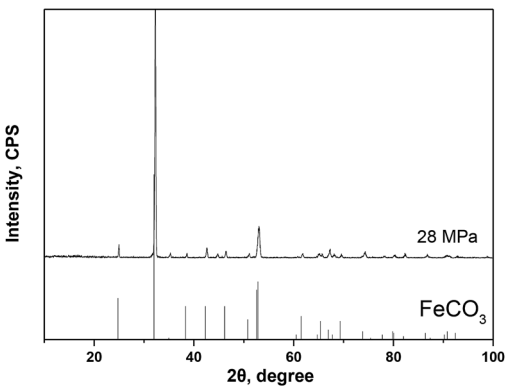

Fig. 5 XRD spectrum of the corrosion film that forms on 13Cr steel surface at 28 MPa.

layer. In region A, a localized pitting is found on the steel surface as shown in Fig. 4c. This is probably related to the local damage of the inner $Cr(OH)_3$ passive film. As shown in Fig. 4c, only $FeCO_3$ particles cover on the steel surface. Corrosive ions, such as Cl^-, can reach to the substrate surface through the gaps between $FeCO_3$ particles. Due to the nonuniformity of the microstructure and composition of the steel substrate, aggressive Cl^- leads to the nucleation of pits on the steel surface which is not covered by $Cr(OH)_3$ passive film.[36] This type of corrosion film is consistent with that forms on 13Cr stainless steel which serves in field under a high-temperature and high-pressure environment.[15]

Cyclic polarization tests

To further understand the pitting and passivation behaviours of 13Cr steel at different conditions. Cyclic polarization measurements were performed in this section. Fig. 6 gives the comparison of cyclic polarization curves of 13 Cr stainless steel at different CO_2 partial pressures. From the forward anodic polarization curves, the 13Cr steel shows a stable passivation at 4 MPa, while it tends to become activate at 28 MPa. Both the pitting potential and the open circuit potential decrease with the increasing of CO_2 partial pressure. Furthermore, the existence of a hysteresis loop in a cyclic polarization curve indicates a delay in repassivation of an existing pit when the potential is scanned cathodically. The larger the hysteresis loop, the more difficult it becomes to repassivate. In our test, the hysteresis loop at 4 MPa is smaller than that at 28 MPa, and the backward scanning curve intersects the cathodic polarization curve. This indicates that the 13Cr steel is more difficult to repassivate and has the lower pitting resistance at 28 MPa.

Discussion

Phase equilibrium under different CO_2 partial pressures

The corrosion rate of 13Cr steel under the CO_2 pressure of 28 MPa is much higher than those under the lower partial pressures. This is related to the incomplete coverage of $Cr(OH)_3$ passive film under 28 MPa as shown in Fig. 4c. To further understand the local damage of the passive film, the pH and different phase concentrations were obtained by phase equilibrium calculation in simulated oil field formation waters under different CO_2 partial pressures.

A water chemistry model of a high-temperature and high-pressure CO_2-saturated solution (open system) is considered in this study. The main homogenous chemical reactions involved in the simulated formation water in this study can be listed as follows.

$$CO_{2(g)} \Leftrightarrow CO_{2(aq)} \quad K_{hen} = c_{CO_2(aq)}/c_{CO_2(g)} \tag{2}$$

$$CO_{2(aq)} + H_2O \Leftrightarrow H_2CO_3 \quad K_{hy} = c_{H_2CO_3}/c_{CO_2(aq)} \tag{3}$$

$$H_2O \Leftrightarrow H^+ + OH^- \quad K_{wa} = c_{H^+}c_{OH^-} \tag{4}$$

$$H_2CO_3 \Leftrightarrow H^+ + HCO_3^- \quad K_{ca} = c_{H^+}c_{HCO_3^-}/c_{H_2CO_3} \tag{5}$$

$$HCO_3^- \Leftrightarrow H^+ + CO_3^{2-} \quad K_{bi} = c_{H^+}c_{CO_3^{2-}}/c_{HCO_3^-} \tag{6}$$

$$CaCO_3 \Leftrightarrow Ca^{2+} + CO_3^{2-} \quad K_{SP,CaCO_3} = c_{Ca^{2+}}c_{CO_3^{2-}} \tag{7}$$

$$MgCO_3 \Leftrightarrow Mg^{2+} + CO_3^{2-} \quad K_{SP,MgCO_3} = c_{Mg^{2+}}c_{CO_3^{2-}} \tag{8}$$

$$FeCO_3 \Leftrightarrow Fe^{2+} + CO_3^{2-} \quad K_{SP,FeCO_3} = c_{Fe^{2+}}c_{CO_3^{2-}} \tag{9}$$

In a high-temperature and high-pressure system, the relationship between the CO_2 concentration and pressure is no longer linear. Thus the Henry's law cannot be used. By comparing different models from literatures used for predicting the CO_2 solubility in a high-temperature and high-pressure system, Duan's model is chosen in this work to get the CO_2 solubility.[36] Fig. 7 gives the solubility of CO_2 under different CO_2 partial pressures.

The equilibrium constant K_{hy} for carbon dioxide hydration does not change substantially with the temperature increasing and it is independent with pressure. Therefore, K_{hy} can be considered as a constant of 1.67×10^{-3}. Both the first-order ionization constant (K_{ca}) and second-order ionization constant (K_{bi}) carbonic acid are the function of temperature and pressure, which can be obtained from the ref. 37.

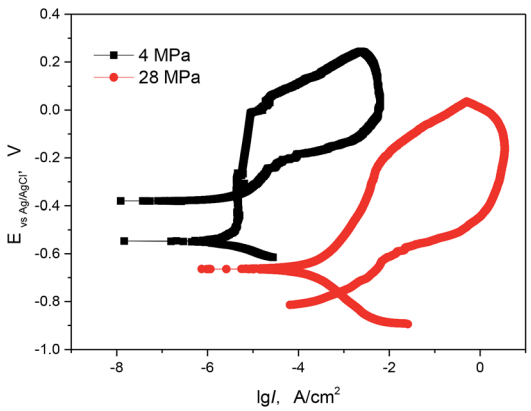

Fig. 6 Cyclic polarization curves of 13Cr stainless steel in a solution with different CO_2 partial pressures at 140 °C.

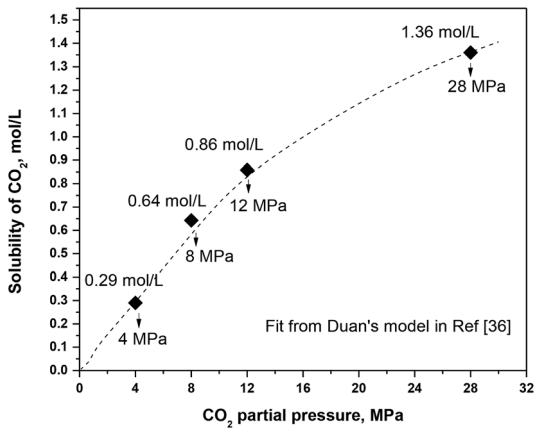

Fig. 7 Solubility of CO_2 under different CO_2 partial pressures.

The other equilibrium constants which include K_{wa}, $K_{sp,CaCO_3}$, $K_{sp,MgCO_3}$, and $K_{sp,FeCO_3}$, can be obtained by the following equations.[38–42]

$$K_{wa} = 10^{-(29.3868-0.0737549\times T+7.47881\times 10^{-5}\times T^2)} \quad (10)$$

$$K_{sp,CaCO_3} = 10^{-7.8156-1502/T+0.03111\times T-5.518\times \lg T} \quad (11)$$

$$K_{sp,MgCO_3} = 10^{7.267-1476.604/T-0.033918\times T} \quad (12)$$

$$K_{sp,FeCO_3} = 10^{175.568-6738.483/T+0.0139\times T-67.898\times \lg T} \quad (13)$$

NaCl, KCl, and $NaSO_4$ completely dissociate in the formation water. The electroneutrality of the solution is independent with these species. Therefore, only the influence of $MgCl_2$, $CaCl_2$, $NaHCO_3$ addition, and the formation of $FeCO_3$ on the hydrolysis equilibrium in CO_2 aqueous solutions is considered. The positive and negative charges are equal in the solution, as expressed in eqn (14).

$$c_{Na^+} + 2c_{Ca^{2+}} + 2c_{Mg^{2+}} + 2c_{Fe^{2+}} + c_{H^+} = c_{OH^-} + c_{HCO_3^-} + 2c_{CO_3^{2-}} + c_{Cl^-} \quad (14)$$

where c_{H^+}, c_{OH^-}, $c_{HCO_3^-}$, $c_{CO_3^{2-}}$, $c_{Ca^{2+}}$, $c_{Mg^{2+}}$, and $c_{Fe^{2+}}$ are the concentrations of H^+, OH^-, HCO_3^-, CO_3^{2-}, Ca^{2+}, Mg^{2+}, and Fe^{2+}, respectively.

By joining eqn (4)–(9) and (14), a quartic equation on c_{H^+} can be obtained as follows:

$$\frac{2(K_{sp,CaCO_3}+K_{sp,MgCO_3}+K_{sp,FeCO_3})}{K_{ca}K_{bi}C_{H_2CO_3}}C_{H^+}{}^4 + C_{H^+}{}^3 + (C_{Na^+} - C_{Cl^-})C_{H^+}{}^2 - (K_{wa}+K_{ca}C_{H_2CO_3})C_{H^+} - 2K_{ca}K_{bi}C_{H_2CO_3} = 0 \quad (15)$$

where $C_{H_2CO_3}$ can be obtained by eqn (3) and Fig. 6; C_{Cl^-} and C_{Na^+} are the concentrations of Cl^- and Na^+ from $MgCl_2$, $CaCl_2$, and $NaHCO_3$, having the values of 0.1315 mol L^{-1} and 0.009836 mol L^{-1}, respectively.

By solving this quartic equation on C_{H^+}, the pH values under different CO_2 partial pressures can be obtained as shown in Fig. 8. Furthermore, by putting C_{H^+} into eqn (4)–(9), the concentrations of each species can be obtained as shown in Fig. 7.

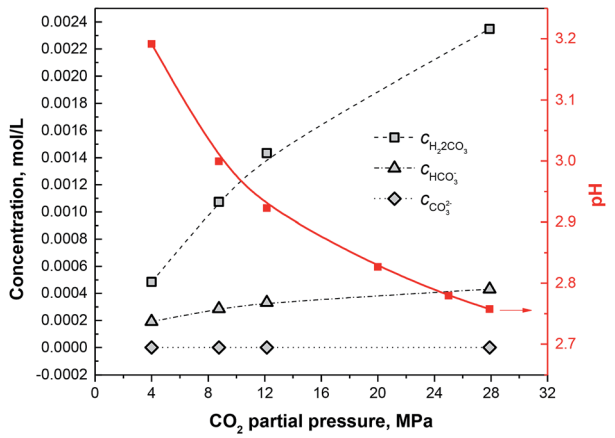

Fig. 8 Concentrations of H_2CO_3, HCO_3^- and CO_3^{2-} and pH plots under different CO_2 partial pressures.

The formation mechanism of the corrosion film on 13Cr steel under different CO_2 partial pressures

Different from the corrosion under the lower CO_2 partial pressures (<12 MPa), a double-layered corrosion film forms on the steel surface when the CO_2 partial pressure increases to 28 MPa. A model is proposed for the film formation on the 13Cr steel surface under different CO_2 partial pressures. As displayed in Fig. 9a, a single-layered passive film forms and completely covers on the steel surface under the lower CO_2 partial pressures. A few scattered $FeCO_3$ particles may forms and deposit on the passive film. The passive film of 13Cr stainless steel mainly consists of $Cr(OH)_3$ which is in amorphous state and could prevent aggressive ions such as Cl^- to transfer to the steel substrate. $Cr(OH)_3$ precipitation contributes to the increase of films thickness and inhibits the precipitation of $FeCO_3$. When the CO_2 pressure reaches 28 MPa, a much different corrosion film which contains an inner $Cr(OH)_3$ passive layer and an outer $FeCO_3$ layer forms on the steel surface as shown in Fig. 9b. What is more interesting is that the inner passive film shows a local damage and the pitting is found under the damaged area. This phenomenon can be explained by the lower pH and the higher H_2CO_3 concentration in the solution under the higher CO_2 partial pressure. Firstly, $Cr(OH)_3$ is soluble in acid. The lower pH can promote the dissolution of $Cr(OH)_3$ passive film. As shown in Fig. 8, the pH of the solution decreases with the increase of CO_2 pressure. The pH under the pressure of 28 MPa

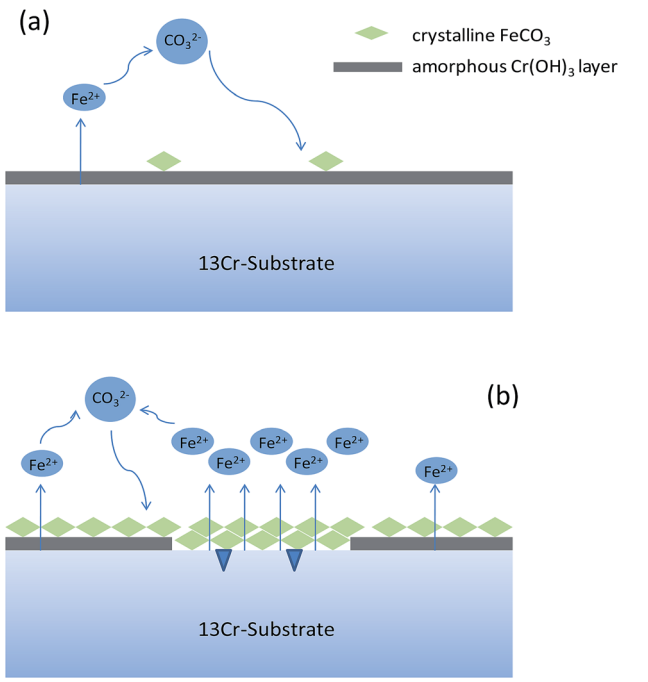

Fig. 9 Schematic diagrams of the corrosion film formation on 13Cr steel surface under different CO_2 partial pressures: (a) 4–12 MPa; (b) 28 MPa.

is the lowest and reaches about 2.75. Therefore, the $Cr(OH)_3$ passive film has the highest dissolution tendency and is the most unstable under the pressure of 28 MPa. Secondly, H_2CO_3 has the dihydroxylation effect on the corrosion film, and thus decrease the stability of the passive film.[24] The H_2CO_3 concentration increases with the increase of CO_2 partial pressure. The H_2CO_3 concentration under the pressure of 28 MPa ($\sim$0.00235 mol L^{-1}) is nearly 4 times higher than that under the pressure of 4 MPa ($\sim$0.00048 mol L^{-1}). The higher H_2CO_3 concentration promotes the dihydroxylation of the passive film and the stability of passive film decreases under the higher CO_2 partial pressure.

In summary, the passive film under the lower pressure (<12 MPa) is stable and protective, thus the corrosion rate keeps at a very low level (see Fig. 1). However, when the pressure increases to 28 MPa, the stability of passive film decreases due to the lower pH and the higher H_2CO_3 concentration. The passive film is easier to be broken and the aggressive Cl^- reaches to the bare steel surface, thus the anodic dissolution of Fe and the nucleation of pits shall be promoted on the steel surface which is not covered by $Cr(OH)_3$ passive film. Moreover, an electrochemical corrosion system with a large cathode and a small anode is established, as shown in Fig. 9b. This will further accelerate the general corrosion and the growth of pit under the damaged area of passive film. Therefore, the corrosion rate shows a sharp increase from 0.00046 mm per year under 12 MPa to 0.011 mm per year under 28 MPa as shown in Fig. 1.

Conclusions

• The 13Cr martensitic stainless steel shows an abrupt change in corrosion resistance if the CO_2 partial pressure increases from 12 MPa to 28 MPa. The corrosion rate under the higher CO_2 pressure is approximately 20–180 times as large as those under the lower CO_2 pressures.

• The stability of the passive film on 13Cr steel surface significantly decreases with the CO_2 partial pressure increases to 28 MPa. Under the lower CO_2 pressures (<12 MPa), a single-layered $Cr(OH)_3$ passive film forms and completely covers on the steel surface. However, when the CO_2 pressure reaches to 28 MPa, a much different corrosion film which contains an inner $Cr(OH)_3$ passive layer and an outer $FeCO_3$ layer forms, and the inner passive layer shows a local damage. This phenomenon can be explained by the lower pH ($\sim$2.75) and the higher H_2CO_3 concentration in the solution under the higher CO_2 pressure. The lower pH and higher H_2CO_3 concentration can promote the dissolution and dihydroxylation of $Cr(OH)_3$ passive film, respectively.

• The 13Cr steel shows higher pitting tendency under the higher CO_2 pressure. This effect is connected with the stability decreasing of passive film. An electrochemical corrosion system with a large cathode and a small anode is established, which will further accelerate the growth of pit under the damaged area of passive film.

Conflicts of interest

There are no conflicts to declare.

Acknowledgements

This work was financially supported by the National Natural Science Foundation of China (no. 51871027) and Fundamental Research Funds for the Central Universities (no. 06500118).

Notes and references

1 R. Barker, Y. Hua and A. Neville, *Int. Mater. Rev.*, 2016, **62**, 1.
2 X. Jiang, Y. G. Zheng, D. R. Qu and W. Ke, *Corros. Sci.*, 2006, **48**, 3091.
3 C. Sun, J. Sun, Y. Wang, X. Lin, X. Li, X. Cheng and H. Liu, *Corros. Sci.*, 2016, **107**, 193.
4 H. Höpfner, *European Federation of Corrosion Publications No. 17*, Maney Publishing, 2nd edn, 2002.
5 H. Marchebois, J. Leyer and B. Orlans-Joliet, in *Corrosion 2007*, NACE International, 2007, paper no. 07090.
6 H. Marchebois, H. E. Alami, J. Leyer and A. Gateaud, in *Corrosion 2009*, NACE International, 2009, paper no. 09084.
7 J. Enerhaug, P. E. Kvaale, M. Bjordal, J. M. Drugli and T. Rogne, in *Corrosion 1999*, NACE International, 1999, paper no. 99587.
8 J. Enerhaug, S. L. Eliassen and P. E. Kvaale, in *Corrosion 1997*, NACE International, 1997, paper no. 97060.
9 L. J. Mu and W. Z. Zhao, *Corros. Sci.*, 2010, **52**, 82.
10 H. Y. Ma, Y. S. He, K. Y. Lee and K. S. Shin, *Key Eng. Mater.*, 2017, **727**, 29.
11 G. Z. Meng, Y. Li, Y. W. Shao, T. Zhang, Y. Q. Wang and F. H. Wang, *J. Mater. Sci. Technol.*, 2014, **30**, 253.
12 J. H. Ding, L. Zhang, M. X. Lu, J. Wang, Z. B. Wen and W. H. Hao, *Appl. Surf. Sci.*, 2014, **289**, 33.
13 S. D. Zhu, J. F. Wei, R. Cai, Z. Q. Bai and G. S. Zhou, *Eng. Failure Anal.*, 2011, **18**, 2222.
14 Z. Zhang, Y. S. Zheng, J. Li, W. Y. Liu, M. Q. Liu, W. X. Gao and T. H. Shi, *Eng. Failure Anal.*, 2019, **95**, 263.
15 Y. Long, G. Wu, A. Q. Fu, J. F. Xie, M. F. Zhao, Z. Q. Bai, J. H. Luo and Y. R. Feng, *Eng. Failure Anal.*, 2018, **93**, 330.
16 Z. F. Yin, X. Z. Wang, L. Liu, J. Q. Wu and Y. Q. Zhang, *J. Mater. Eng. Perform.*, 2011, **20**, 1330.
17 K. Krishnan, in *Corrosion 2017*, NACE International, 2017, paper no. 9645.
18 M. D. Pereda, C. A. Gervasi, C. L. Llorente and P. D. Bilmes, *Corros. Sci.*, 2011, **53**, 3934.
19 X. W. Lei, H. Y. Wang, F. X. Mao, J. P. Zhang, M. F. Zhao, A. Q. Fu, Y. R. Feng and D. D. Macdonald, *Corros. Sci.*, 2018, **131**, 164.
20 B. W. Luo, J. Zhou, P. P. Bai, S. Q. Zheng, T. An and X. L. Wen, *Int. J. Miner., Metall. Mater.*, 2017, **24**, 646.
21 X. W. Lei, H. Y. Wang, N. Wang, D. Z. Ren, A. Q. Fu, C. X. Yin, J. P. Zhang, Y. R. Feng and D. D. Macdonald, *Appl. Surf. Sci.*, 2019, **478**, 255.
22 S. Pahlavan, S. Moazen, I. Taji, K. Saffar, M. Hamrah, M. H. Moayed and S. M. Beidokhti, *Corros. Sci.*, 2016, **112**, 233.
23 X. C. Han, J. Li, K. Y. Zhao, W. Zhang and J. Su, *J. Iron Steel Res. Int.*, 2013, **20**, 74.

24 J. Banaś, U. Lelek-Borkowska, B. Mazurkiewicz and W. Solarski, *Electrochim. Acta*, 2007, **52**, 5704.
25 H. Y. Li, C. F. Dong, K. Xiao, X. G. Li and P. Zhong, *Int. J. Miner., Metall. Mater.*, 2016, **23**, 1286.
26 M. Kimura, Y. Miyata, T. Toyooka and Y. Kitahaba, *Corrosion*, 2001, **57**, 433.
27 R. D. Kane and J. Burman, in *Corrosion 2012*, NACE International, 2012, paper no. 1137.
28 Y. Liu, L. N. Xu, M. X. Lu, M. Yao, J. Y. Zhu and L. Zhang, *Appl. Surf. Sci.*, 2014, **314**, 768.
29 L. Calabrese, L. Bonaccorsi, M. Galeano, E. Proverbio, D. Pietro and F. Cappuccini, *Corros. Sci.*, 2015, **98**, 573.
30 X. Zhong, S. C. Bali and T. Shoji, *Corros. Sci.*, 2017, **118**, 143.
31 *ASTM G1-03*, ASTM, West Conshohocken, PA, 2011.
32 S. Q. Guo, L. N. Xu, L. Zhang, W. Chang and M. X. Lu, *Corros. Sci.*, 2012, **63**, 246–258.
33 J. Y. Zhu, L. N. Xu and M. X. Lu, *Corrosion*, 2015, **71**, 854.
34 W. J. Landis and J. R. Martin, *Int. J. Miner. Process.*, 1994, **42**, 251.
35 G. S. Frankel, *J. Electrochem. Soc.*, 1998, **145**, 2186.
36 Z. H. Duan and D. D. Li, *Geochim. Cosmochim. Acta*, 2008, **72**, 5128.
37 R. C. Weast, *Handbook of chemistry and physics*, CRC Press, Florida, 2001.
38 M. Nordsveen, S. Nesic, R. Nyborg and A. Stangeland, *Corrosion*, 2003, **59**, 443.
39 G. Dorange, A. Marchand and M. Le Guyader, *J. Water Sci.*, 1990, **3**, 261.
40 P. Bénézeth, G. D. Saldi, J. L. Dandurand and J. Schott, *Chem. Geol.*, 2011, **286**, 21.
41 P. Bénézeth, J. Dandurand and J. Harrichoury, *Chem. Geol.*, 2009, **265**, 3.
42 X. P. Li, Y. Zhao, W. L. Qi, J. F. Xie, J. D. Wang, B. Liu, G. X. Zeng, T. Zhang and F. H. Wang, *Appl. Surf. Sci.*, 2019, **469**, 146.